Measurements of Temperature Fluctuations in Breaking Surface Waves

DAVID M. FARMER AND JOHANNES R. GEMMRICH*

Institute of Ocean Sciences, Sidney, British Columbia, Canada

27 January 1994 and 25 September 1995

ABSTRACT

Measurements of temperature fluctuations and air entrainment within the upper 1 m of the surface caused by breaking surface waves have been acquired with a novel surface-following sensor array. Brief temperature fluctuations of order 20 mK–100 mK lasting up to 1.5 s and coincident with wave breaking are observed. Although a few of the temperature fluctuations represent direct measurements of the temperature of entrained air in large bubbles, it appears that in many cases the disruption of the ocean thermal boundary layer and its vertical mixing is observed. The observations suggest that wave breaking may play a role in the vertical mixing of warm or cool water stored in the top few centimeters near the ocean surface to depths at which more persistent structures continue the process. Only about 30% of whitecaps exhibit this temperature fluctuation. The authors hypothesize that measurable thermal injections tend to be concentrated in Langmuir convergence zones, which accentuate the thickness of the ocean thermal boundary layer.

1. Introduction

While breaking waves are known to be an important mechanism for the transfer of gas (Thorpe 1982; Kitaigorodskii 1984; Woolf and Thorpe 1991; Farmer et al. 1993; Keeling 1993), momentum (Melville and Rapp 1985; Lamarre and Melville 1991), and salt and water droplets (Bortkovskii 1987; Ling 1993) between the atmosphere and ocean, their role in the vertical transfer of heat is less clear. Most of the heat exchanged between atmosphere and ocean must occur through processes occurring within the ocean thermal boundary layer (e.g., Katsaros 1980), solar radiation being the primary exception. While temperature anomalies associated with the surface skin (e.g., Hasse 1971) have received attention because of their significance to remote sensing (e.g., Schluessel et al. 1990), vertical heat transfer from the upper few centimeters into deeper water remains poorly understood. Thorpe and Hall (1987) made thermistor measurements with a towed spar. They reported temperature anomalies of 10 mK coincident with bubble clouds at depths $\geq$ 2.4 m but could not unambiguously distinguish between Langmuir circulation and breaking waves as the cause of observed fluctuations. Here we report preliminary measurements of temperature fluctuations in the upper 1 m of the water column, showing that they are coincident with air entrainment due to breaking surface waves.

2. Observations

Our measurements were obtained in Georgia Strait (124°48′W, 49°48′N) in November 1991 using a freely drifting instrument (Fig. 1a) supporting four 4-electrode conductivity cells and four Thermometrics FP07 fast-response thermistors (response time 7 ms in water) at depths of 0.17 m, 0.32 m, 0.51 m, and 0.67 m. Sensor resolutions were $2 \times 10^{-4}\ \Omega^{-1}\ m^{-1}$ and 2 mK respectively, with an effective sampling rate after filtering of 32 Hz. The sensor support is connected by hinged arms to the main housing containing batteries and a recording system and has a 0.033-m^3 ethafoam float fixed to it so as to keep the sensors at a nearly constant depth beneath the surface. Electrical conductivity is a convenient measure of the brief ($\sim$1 s) but large air entrainment fractions ($\geq$0.01) within and directly beneath breaking surface waves (Lamarre and Melville 1992). For our sensor design the sensitive volume is approximately a sphere of radius 9 cm. Available theory relating conductivity to void fraction breaks down for large values (>0.5) (Olsen 1967). However, for small values we could verify the sensor response in a calibration tank where air fractions up to 0.25 could be realized. A drogue keeps the sensors pointing into the wind, thus minimizing disturbance to the measured properties. Video cameras scan the measured field from above and beneath the surface (Figs. 1b,c) and were used to verify the surface-following properties of the

* Additional affiliation: University of Victoria, Victoria, British Columbia, Canada.

Corresponding author address: Dr. David M. Farmer, Institute of Ocean Sciences, P.O. Box 6000, 9860 West Saanich Rd, Sidney, BC V8L 4B2, Canada.
E-mail: dmf@IOS.BC.CA

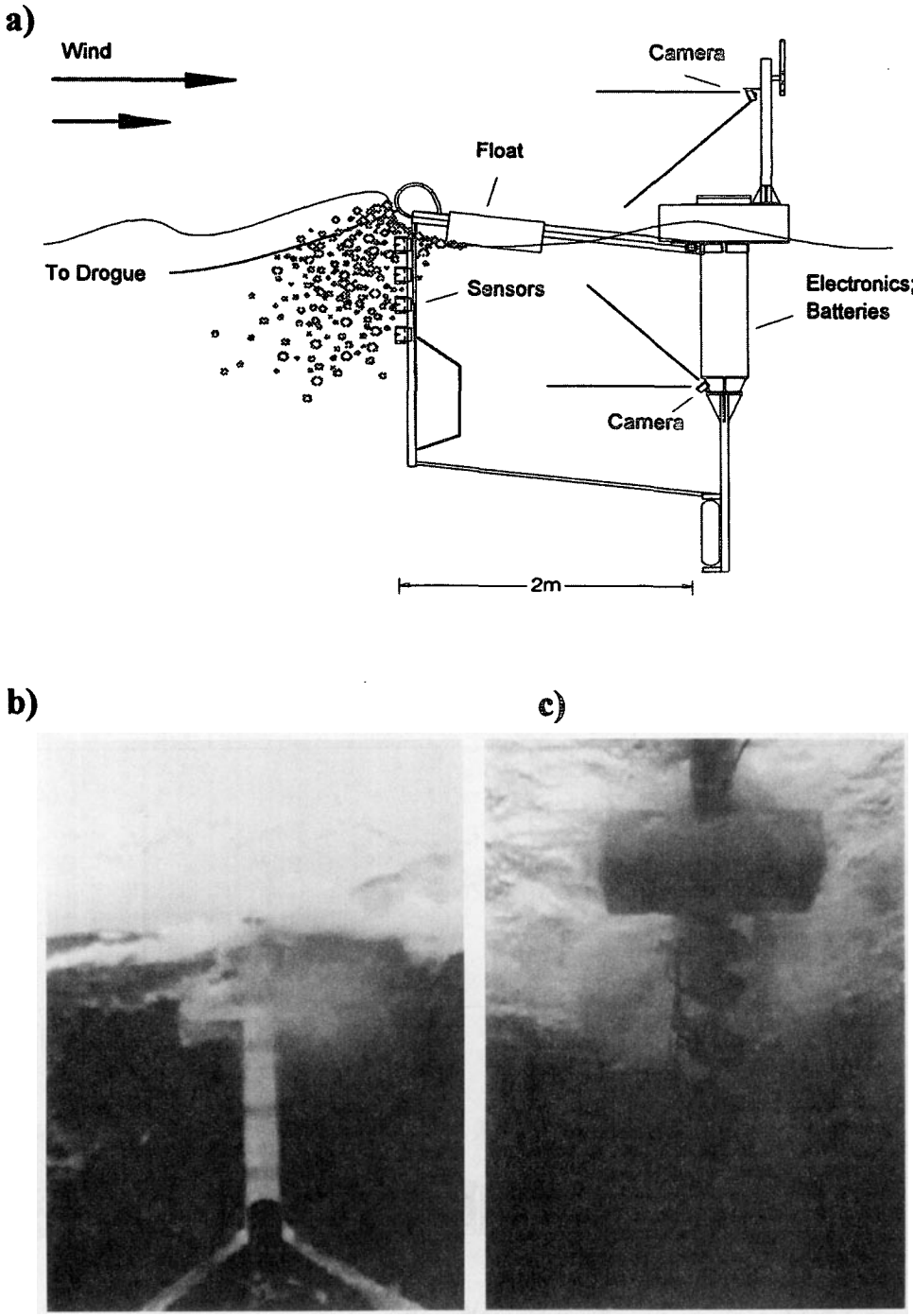

FIG. 1. (a) Self-contained instrument for measurement of breaking waves and surface layer thermal processes. (b) Video images from above and (c) beneath the surface, corresponding to the wave breaking event shown in Fig. 3a. In (c), the two upper sensors are just on the point of being surrounded by bubbles, shortly before disappearing from view.

sensor array and to confirm the interpretation of high void fractions as breaking waves.

Meteorological conditions were obtained from a nearby meteorological buoy with additional information of dewpoint, precipitation, and cloud cover from Comox Airport, approximately 15 km southwest of the measurement site. The wind was from the southeast throughout the deployment with speeds close to 14

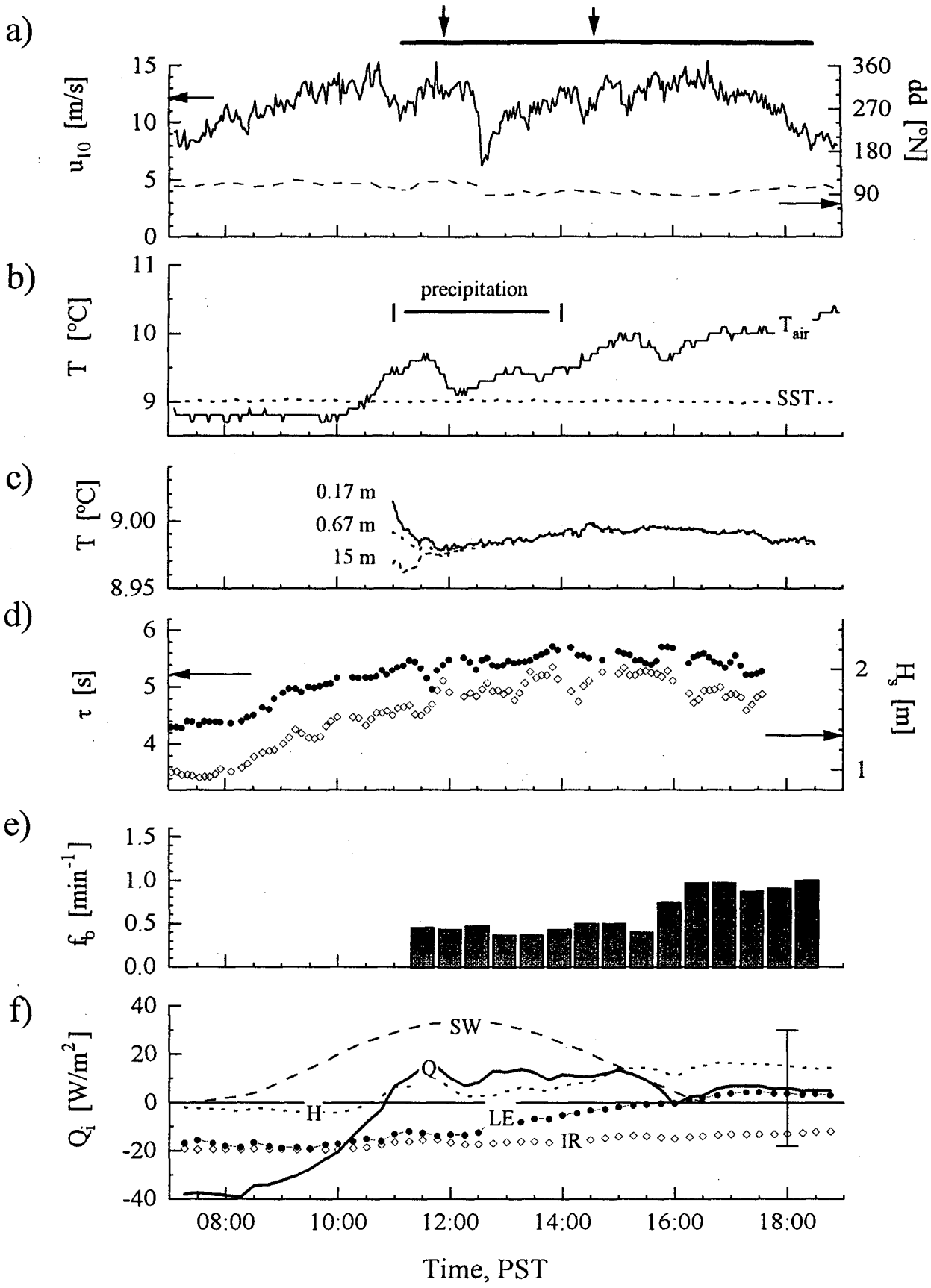

m s^{-1} (Fig. 2a). The fetch was approximately 20 km. The air–sea temperature difference was slightly negative during the morning but changed sign at 1030 h and thereafter remained positive throughout the deployment, increasing to 1.5 K toward the end (Fig. 2b,c). Rain showers were recorded at Comox between 0400 and 1000 (all times local) with a total precipitation of 1.6 mm, but continuous rainfall contributed 7.1 mm of precipitation from 1100 to 1400. Thereafter the rain tapered to showers again and contributed a further 1.5 mm of precipitation by the end of the deployment. The wave field and bubble distribution was monitored by a nearby inverted echo sounder and acoustic imaging system. Significant wave height was 1.6–2.1 m and the dominant wave period was 5.0–5.7 s (Fig. 2d). Figure 2e shows the wave breaking frequency obtained from the number of events exhibiting more than 8% air fraction at the 0.17-m-deep conductivity sensor. The threshold of 8% air fraction as definition of a breaking wave was chosen for consistency with theoretical findings (Longuet-Higgins and Turner 1974). Wave breaking frequencies rise from 0.5 to 1 min^{-1}. The nondimensional breaking frequency, defined as the number of breaking waves per dominant wave, ranges between 0.02 and 0.1. For the observed ratio between wind speed and dominant phase speed (1.1–1.7) the breaking frequency is slightly higher than obtained in other investigations (e.g., see Thorpe 1993).

Bulk estimates of the heat flux components (Fig. 2f) are subject to considerable uncertainty but indicate a change from cooling to warming during the storm (Fig. 2c). Exchange coefficients for latent and sensible heat were derived from tables by Smith (1981), and shortwave radiation was calculated from solar elevation and cloud coverage (Dobson and Smith 1988) neglecting the fraction absorbed below the thermal boundary layer. Net infrared radiation was estimated from air–sea temperatures, cloud coverage, and humidity (Efimova 1961). The contribution to the heat flux by rain [assumed to have the wet-bulb temperature of the air (Katsaros 1976)] is estimated at less than 5 W m^{-2} and was therefore neglected. The radiative fluxes are the least well known, contributing to an uncertainty in net heat flux Q of up to ± 20 W m^{-2}. This introduces some uncertainty in the time at which the heat flux changes sign.

For most of the storm the temperature series at 0.17–0.67 m follows the same pattern of variation as that at 15 m obtained with a nearby recording CTD. However, there is evidence from the thermistor time series (Fig. 2c) of cooling of at least the upper 0.67 m for a brief period (1110–1150) at the beginning of the deployment. Between 0900 and 1800 calculation of the heat and salt budgets of the deepening mixed layer shows that a one-dimensional representation is reasonable (Farmer et al. 1993). However, prior to 0900 h significant advection occurred, and this is likely to account for what is evidently a complex near-surface thermal structure prior to 1000 h. The 0.17-m and 0.67-m thermistors show a positive gradient of 18 mK, which disappears after 1200 h. At the same time large negative temperature anomalies are associated with wave breaking. A likely explanation is that a thin salinity-stabilized surface layer resulting from previous advection had cooled during the preceding period of heat loss, was augmented by precipitation, and subsequently became the source of cooler water appearing during breaking wave injections. The gradual evolution of the temperature over the measured period has been shown to be dominated by entrainment effects.

Figure 3a shows an example of the air fraction and temperature anomaly associated with a single breaking event, which is the same as that reproduced in the video image (Fig. 1b). A temperature drop of ~250 mK occurs at 0.17 m, decreasing to 4 mK at the deepest sensor (0.67 m). The air fraction measurement saturates (0.65) for the shallowest sensors in this example, decreasing to <0.1 at the deepest (0.67 m). However, our calibration is limited to air fractions <0.25, and even in the absence of saturation large values can only be considered as approximate. The entire breaking event lasts ~1 s. Negative temperature anomalies occur only for the first hour of the deployment. Figure 3b shows another example obtained a few hours later. A similar air penetration occurs, but this time with a maximum positive temperature fluctuation of 34 mK. When they occur, temperature fluctuations are coincident with wave breaking events. However, only 28% of breaking events exhibit a temperature signal exceeding the background noise level (rms 2.3 mK).

In 17 of the 98 cases observed with temperature fluctuations greater than 10 mK, the temperature signal is

FIG. 2. Environmental conditions for the Strait of Georgia deployment (49°48′N, 124°48′W), on 24 November 1991. (a) Wind speed corrected to 10 m and direction. The horizontal bar indicates the duration of the instrument deployment and the two vertical arrows mark the breaking events shown in Figs. 3a,b. (b) Air temperature T_{air} and water temperature SST and time of major precipitation. (c) Thermistor time series at 0.17 m (solid) and 0.67 m (dotted) depth, and at 15 m (dashed) obtained from a nearby recording CTD. All curves were superimposed to match the CTD value at 1500 h, thus offsetting thermistor calibration uncertainties. (d) Dominant wave period τ (solid symbols) and significant wave height H_s (open symbols). (e) Breaking wave frequency f_b measured with conductivity sensor at 0.17 m. (f) Components of bulk heat flux estimates including latent LE and sensible H heat fluxes and net infrared IR and shortwave radiation SW. SW excludes 60% of the total shortwave radiation that is absorbed beneath the thermal boundary layer. The net heat flux Q is defined as $Q = (1 - \alpha)\, SW + H + LE + IR$, where α is the surface albedo.

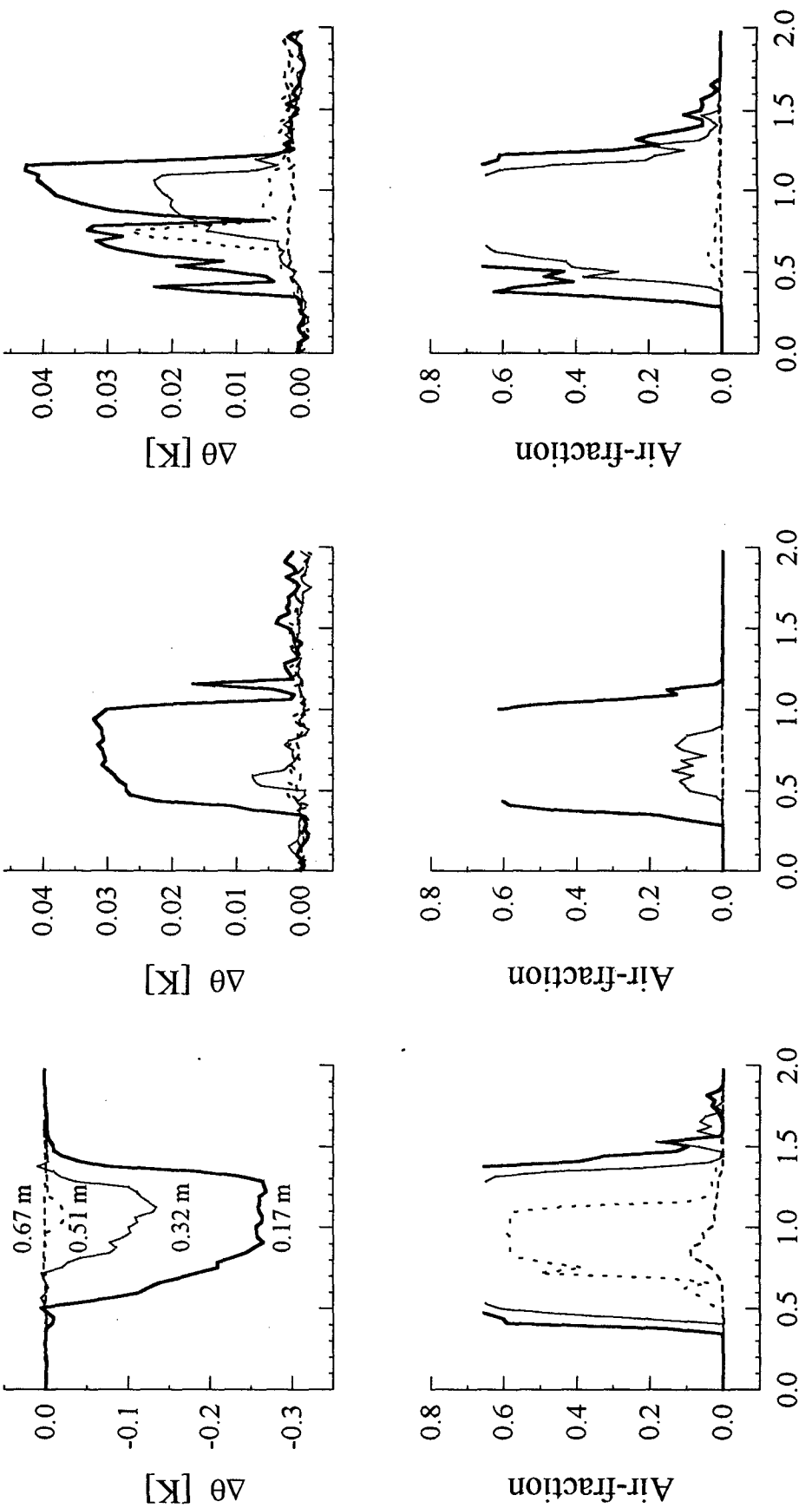

FIG. 3. (a) Temperature anomaly (above) and air fraction (below) measured by sensors at 0.17 m, 0.32 m, 0.51 m, and 0.67 m during the event shown in Figs. 1b,c. Note that temperature anomalies > 100 mK were observed only during times of precipitation. Air fraction values > 0.5 exceed the range of valid theory for the sensors and should be considered only as indication of air content. (b) Same as Fig. 3a but at a later period when the anomalies were positive (note scale change). (c) Same as Fig. 3b but for a case where large bubbles influence the temperature record.

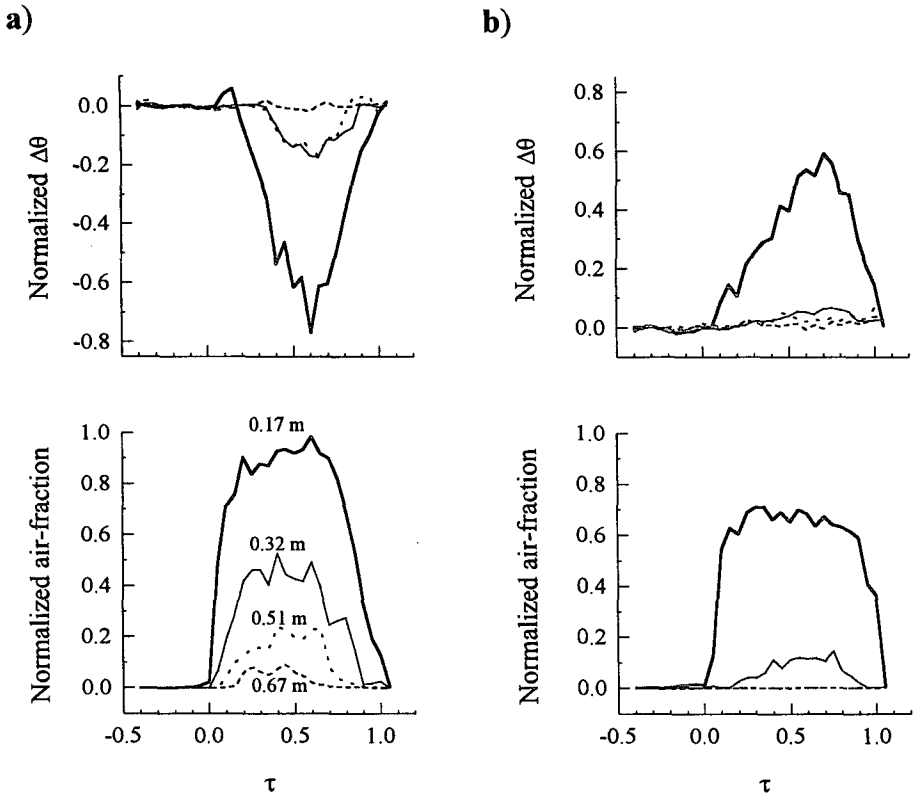

FIG. 4. (a) Above: Average temperature anomalies for the cooling period (1110–1220 h) where the temperature fluctuation has been normalized by its maximum value and the time scaled by the event duration as detected by the 0.17-m conductivity cell. Below: Corresponding average air fractions normalized by their maximum value and timescaled by event duration. (b) As for Fig. 4a, but for the warming period 1500–1830 h.

quite different from the others. In these cases rapid fluctuations occur, each segment of which involves initially a fast change that then slows as it approaches a final value before returning sharply to the background level. An example is shown in Fig. 3c. This behavior is quite different from the more continuous variation exhibited in the remaining 81 examples, and also for those events showing temperature fluctuations less than 10 mK. For reasons discussed in more detail below, these examples are believed to represent measurements of air temperature in large bubbles or in very high void fractions rather than water temperature and are excluded from subsequent analysis. In most cases, however, the thermistors appear to record a signal that is dominated by water temperature.

In very steep waves it is possible that the uppermost sensor (0.17 m) breaks through the surface and gets exposed to air. However, this transition at the surface to extreme low conductivity causes a very distinctive pattern of the conductivity reading, which can readily be identified, and these cases are not included in the analyzed dataset.

Figures 4a,b show averaged temperature anomalies (above) and averaged air fraction (below) for periods of negative and positive signal. Each sample is normalized by the maximum values encountered during the breaking event and is scaled by duration of air entrainment, prior to averaging.

The normalized temperature anomaly falls off rapidly with depth, but there is a slight tendency for the maximum value to occur toward the end of the event. It seems that this slight lag in the temperature fluctuation is a relatively common feature of these data occurring in 62% of the observed cases. A possible explanation of this tendency lies in the hydrodynamically active behavior of the bubbles. Air rising to the surface will be replaced by the surface water. Since the flow is subject to strong vertical shear, toward the end of the breaking event some of the bubbles may rise into the surface water that lies just upwind of the area that has been mixed; thus, the bubbles rise into water that is still thermally stratified. When this happens, thermally anomalous water is mixed down, but not as deeply as at the start of the wave breaking, and appears as a max-

imum in the temperature anomaly. The present dataset does not allow unambiguous validation of this hypothesis.

Although the temperature time series at different depths during periods *between* wave breaking events have almost identical slowly fluctuating variability, small discrepancies occur at higher frequencies (i.e., >0.01 Hz). If we superimpose the series to offset calibration uncertainties at this level, we find the difference in the time series outside breaking events between 0.17 and 0.32 m is 0.5 mK rms, but is 1.8 mK rms between 0.32 and 0.67 m. This suggests the presence of a small, but not directly measurable, temperature gradient close to the surface.

3. Discussion

Event-averaged temperature anomalies (Fig. 5a) change from strongly negative to slightly positive at 1220 h. In the vicinity of a breaking wave, the thermal boundary layer is mixed downward. The heat capacity per unit volume (ρc_p) of water is more than 3000 times that of air, so that the heat contribution of the bubbles in the air–water mixture is negligible. However, the time it takes for the air bubble temperature to equilibrate with the surrounding water depends on the bubble size. This equilibration time may exceed the time it takes for the bubble to reach the sensor. A lower bound on the bubble injection speed can be inferred from the delay of the onset of the conductivity signal between the two shallowest sensors and their spatial separation, under the assumption that the bubbles are traveling vertically with respect to the sensors. The inferred speeds vary from 0.4 to 1.9 m s^{-1} with a median value of 0.9 m s^{-1}. Koga (1982) measured the speed of bubble entrainment in a wave tank at a wind speed of 16 m s^{-1} and found values between 0.4 and 1.2 m s^{-1}. Thus we take 0.2 s as the minimum time bubbles need between their formation and their arrival at the thermistor depth. In the appendix we model the equilibration process and show that only bubbles larger than 6-mm diameter will fail to equilibrate to the water temperature within this bubble transit time. For larger bubbles the thermistor response depends upon bubble size, flow speed, and bubble separation. The model also illustrates the distinctive character of the signal from air temperature measurements in large air bubbles consistent with the 17 examples identified in the dataset. For all other examples we conclude that the observed temperature signal is not significantly influenced by the temperature within the air bubbles.

A simple mixing argument allows us to investigate the potential role of wave breaking in the vertical transport of heat. Suppose that the heat anomaly is stored in a thin surface layer of thickness ϵ and temperature anomaly θ_ϵ, where ϵ is much less than the depth z_m of the shallowest sensor. When air is entrained, we assume uniform mixing of this thin water layer down to a depth

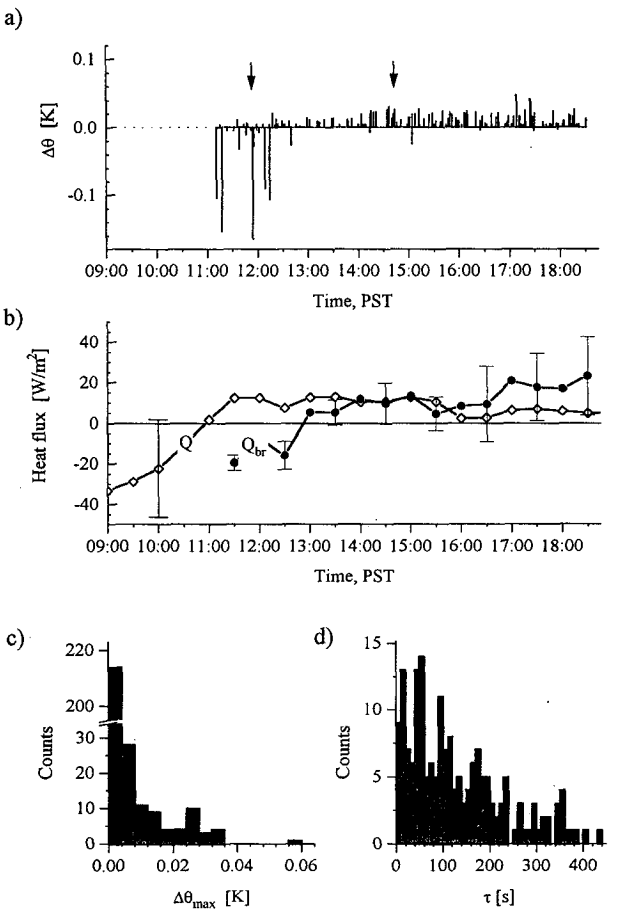

FIG. 5. (a) Time series of event-averaged temperature anomalies detected by the 0.17-m thermistor. Arrows identify events shown in Figs. 3a,b. (b) Breaking-wave-induced heat flux Q_{br} derived from (2), and bulk estimate of effective air–sea flux Q. (c) Histogram of maximum temperature anomalies $\Delta\theta_{max}$ at 0.17 m for the period 1500–1800 local time. (d) Histogram of time delay between breaking events with temperature signal.

z_m, so that the heat transported past the depth ϵ would be

$$W = \rho_m c_{p_m} \theta_m (z_m - \epsilon), \qquad (1)$$

where ρ_m is the density, c_{p_m} is the specific heat, and θ_m is the temperature anomaly of the air–water mixture at depth z_m.

For $\epsilon \ll z_m$, the heat flux per unit area from the thermal boundary layer to deeper water due to a total of N wave breaking events would then be

$$Q_{br} = \frac{\gamma}{N} \sum_{i=1}^{N} \left[\frac{1}{\tau z_m} \int_0^{z_m} \int_0^{\tau} \rho_m c_{p_m} \theta_m z \, dt \, dz \right]_i, \qquad (2)$$

where γ is the breaking frequency, τ is the duration of a breaking event, and ρ_m, c_{p_m}, θ_m are functions of time and depth. Figure 5b shows a comparison of the heat flux estimated by bulk methods with the breaking-

wave-induced heat flux derived by trapezoidal integration of (2). Notwithstanding large error bounds in Q, the limitation of conductivity measurements for large void fractions mentioned above, and the limitations of our assumption of uniform mixing, both time series exhibit a shift from cooling to warming and are of similar magnitude. Much larger anomalies occurring before 1230 h may result from the stabilizing effect of precipitation (Katsaros 1976), which would reduce vertical mixing between breaking events.

The surface shear and an average instrument drift of 0.3 m s^{-1} ensure that successive breaking waves do not mix the same area detected in the preceding event if the time delay is more than approximately 7 s. Furthermore, the recovery time of the cool skin has been measured following its destruction by a breaking wave and found by an infrared imager to be approximately 1 s (Jessup 1996), and by radiometer (Clauss et al. 1970) to be 10 s. This rapid recovery time shows that the thermal skin is only briefly interrupted by breaking. However, the distribution of temperature anomalies (Fig. 5c) reveals that ~70% of events exhibit no measurable temperature anomaly at all. If the observed distribution is representative of breaking wave occurrence and resulting temperature fluctuations, we infer that within two-thirds of the surface area the thermal boundary layer is too thin to be detected following mixing to the depths of our sensors.

It has long been known that infrared images of the ocean surface exhibit streaklike features in the surface temperature field, commonly associated with Langmuir circulation (McAlister and McLeish 1965). We anticipate that this circulation advects the thin surface layer along with its heat surplus or deficit. Advection would cause the thermal boundary layer thickness to vary depending on location relative to the Langmuir convergence zone. This advection would apply equally to a thin surface layer of freshwater due to precipitation. Breakers within the convergence zone would produce a small temperature deviation, whereas those between convergence zones would produce little or no signal.

Our instrument drifted at 0.25 m s^{-1} across the wind and therefore traversed successive Langmuir convergence zones (Fig. 6). At this time the mean Langmuir cell spacing was d_m = 18.3 m (Farmer and Li 1995), the corresponding transit time would therefore be approximately 55 s, with the sensor spending ~20 s within each convergence zone. If temperature anomalies ($\Delta\theta$ event) are only detected within these zones, there is an increased probability that the time separation between successive $\Delta\theta$ events will be either less than 20 s or a multiple of 55 ± 10 s. For the separation of ~30 s or ~80 s, the probability of $\Delta\theta$ events is low. Our limited dataset precludes unambiguous detection of clustering expected within convergence zones. However, peaks in the probability distribution (Fig. 5d) at 20, 50–60, 100–120, and 170 s are consistent with the hypothesis that $\Delta\theta$ events are confined to convergence zones.

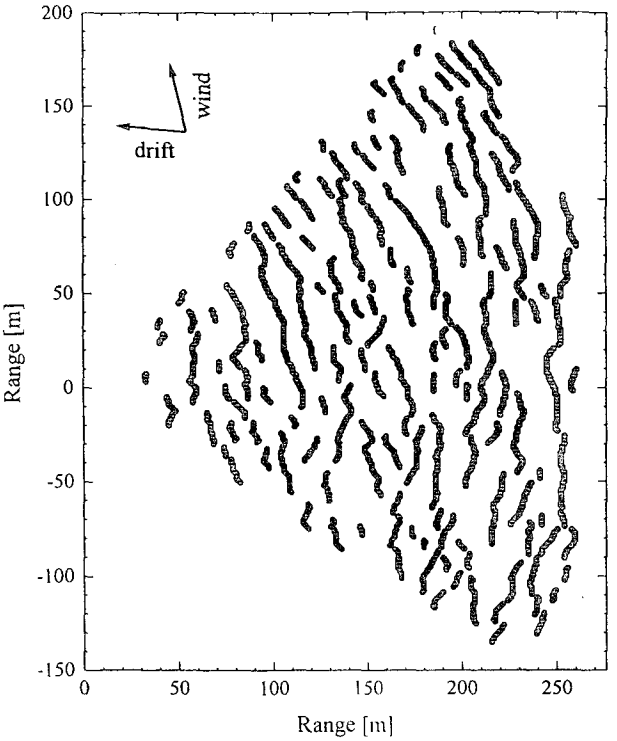

FIG. 6. Bubble cloud patterns derived from a scanning sonar image at 1139 using the method of Farmer and Li (1995), showing a two-dimensional view of bubble clouds organized by Langmuir circulation. The arrows indicate wind direction and the mean direction of instrument drift.

These observations reveal quite significant temperature fluctuations within breaking waves. While the effect of air–sea temperature differences complicate the measurement, it appears that measurable effects result from vertical mixing of heat surplus or deficit stored in the upper few centimeters. Our observations are consistent with the concentration of near-surface thermal anomalies in Langmuir convergence zones. Breaking waves enhance air–sea exchange of gas and momentum; these observations suggest that they may also play a role in the air–sea exchange of heat.

Acknowledgments. This work was supported by the Canadian Joint Global Ocean Flux Study, the U.S. Office of Naval Research, and the Canadian Panel on Energy Research and Development. We thank A. Adrian and D. Lapshinoff for assistance with the instrument development and deployment, and Drs. A. D. Booth and P. Craig and a reviewer for helpful comments.

APPENDIX

Thermistor Reading in Air–Water Mixture

The apparent temperature cross section in a bubbly air–water mixture detected by a thermistor depends

mainly on three parameters: 1) the equilibration of air to the surrounding water temperature, 2) the time response of the thermistor in air, and 3) the time response of the thermistor in water.

Following formation of an air bubble within water of different temperature, diffusion of heat through the bubble skin and within the air bubble will tend to equalize the temperature. The rate at which equilibrium is approached depends upon the heat diffusivity and bubble radius. Since the water temperature does not change significantly due to heat transfer from the bubble, it may be taken as constant for the purpose of calculation. The equilibration process is described by diffusion for a sphere:

$$\frac{\partial T}{\partial t} = \frac{k_t}{r^2}\frac{\partial}{\partial r}\left(r^2\frac{\partial T}{\partial r}\right), \tag{A1}$$

$$T = \begin{cases} 0 & \text{for} \quad r < a, t = 0 \\ T_a & \text{for} \quad r = a, t \geq 0, \end{cases}$$

where a is the radius of the bubble, T_a the water temperature, and k_t the thermal diffusivity of air. Note that this neglects mixing of air within the bubble and therefore leads to an upper bound on the calculated time taken to reach equilibrium. The solution for the average temperature T_{av} in the bubble is (Carslaw and Jaeger 1959)

$$\frac{T_{av}}{T_a} = 6\sqrt{\frac{\zeta}{\pi}} - 3\zeta + 12\sqrt{\zeta}\sum_{n=1}^{\infty} i\text{erfc}\,\frac{n}{\sqrt{\zeta}},$$

$$\zeta = \frac{k_t t}{a^2}. \tag{A2}$$

Figure A1 shows the temperature equilibration of bubbles as a function of time in a nondimensional form, according to Eq. (A2). For an initial temperature of the bubble 0.5 K higher than the water temperature, corresponding to our average deployment conditions and $k_t = 2.0 \times 10^{-5}$ m^2 s^{-1}, it is seen that only bubbles with a diameter larger than 6 mm take more than 0.2 s (the estimated minimum time for the bubble to reach the sensor depth) to equilibrate to within 1%. However, larger bubbles with diameter greater than 10 mm show significant temperature deviations up to a time of 0.5 s after injection.

The response of a thermistor to a steplike temperature change is governed by the heat transfer equation

$$\frac{dT}{dt} = -\frac{T - T_A}{\tau} \tag{A3}$$

with solution

$$T = T_A + (T_i - T_A)e^{-t/\tau}, \tag{A4}$$

where T_i is the initial temperature of the thermistor, T_A is the ambient temperature, and τ is the thermal time

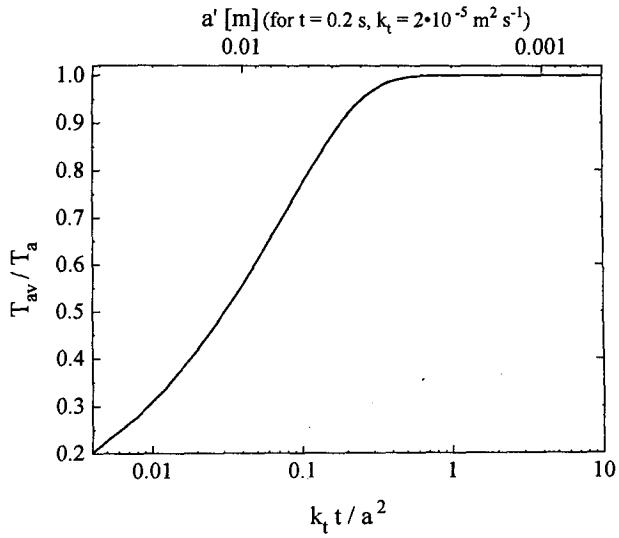

FIG. A1. Temperature equilibration of a sphere of temperature T_{av} to the surrounding temperature T_a as a function of radius a, time t, and diffusivity k_t. At the top of the figure, the scale is shown for radius a' in the case of air bubbles with $k_t = 2.0 \times 10^{-5}$ m^2 s^{-1} after a time $t = 0.2$ s. For example, a 3-mm radius bubble would reach equilibrium within the 0.2-s period.

constant of the device. Here τ is specified by the manufacturer as $\tau = 0.1$ s in air and $\tau = 0.007$ s when the thermistor is in water.

We modeled the apparent temperature reading of our thermistor type in an air–water mixture of spherical bubbles of uniform size. The initial air temperature was set to be 0.5 K higher than the water temperature, and we assumed no bubble would reach the thermistor depth within the first 0.2 s. The separation of adjacent bubbles was fixed at 1 mm. This represents a rather extreme example in which all the bubbles are perfectly aligned. Since the thermistor will be covered with a thin water layer even within the air bubble, the thermal time constant in air has to be increased. An estimate for the thermal time constant of a wet thermistor of $\tau = 0.2$ s was obtained from dockside tests in which the thermistor breaks the water surface. Note that the additional air flow in the atmospheric boundary layer reduces τ toward a lower value than expected within an air bubble. A time step corresponding to our original sampling frequency of 687 Hz was chosen. The bubbles are advected past the thermistor by a constant flow speed v_d, which is dominated by the rise speed of the bubbles. The rise speed is a function of bubble size and contamination of the water and ranges for bubbles of diameter 1 mm to 20 mm between 0.2 m s^{-1} and 0.3 m s^{-1} (Cliff et al. 1978), although it should be recognized that advection may often be more important than bubble rise speed in still water.

Figure A2 shows temperature deviations as seen by the thermistor for three different bubble sizes and two different flow speeds. Due to the short equilibration time of small bubbles, essentially no temperature anomaly would

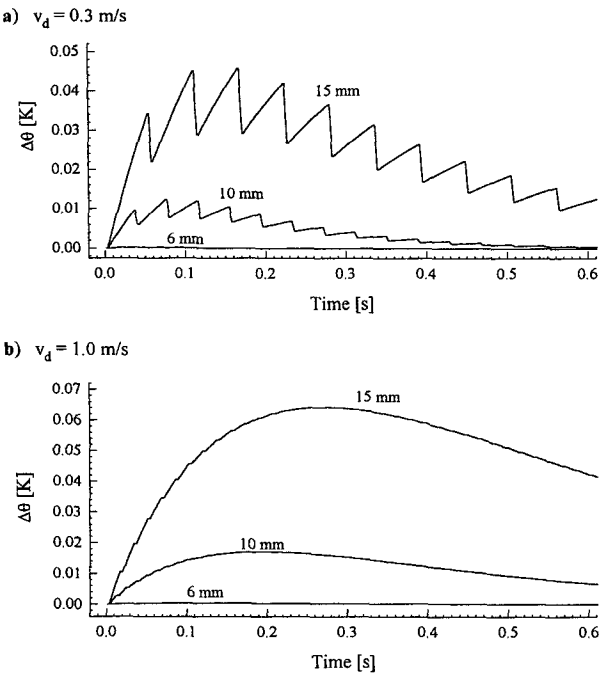

FIG. A2. Modeled temperature record of the thermistor in air bubbles of stated diameter separated by 1 mm of water. The temperature of the air bubble was initially 0.5 K higher than the water temperature and prior to the 0.2-s transit time to the thermistor. (a) For a bubble flow speed $v_d = 0.3$ m s^{-1}, (b) for $v_d = 1.0$ m s^{-1}.

be recorded at our sensor depth under the assumptions stated above for a bubble diameter less than 6 mm. Bubbles with a diameter of 10 mm or larger are still noticeably warmer than the surrounding water, and the time needed to traverse the bubble is long enough for the thermistor to respond. For a 1-mm separation between bubbles, the water layer between adjacent bubbles is not thick enough to cool the thermistor completely down to the water temperature resulting in a sawtoothlike temperature curve. It is this mechanism that is most probably responsible for the structure seen in Fig. 3c. For an increased flow speed of $v_d = 1$ m s^{-1}, the time spent between bubbles is too short to allow the thermistor to respond, and therefore the air temperature would be recorded. However, there is strong evidence from observational and theoretical work (Longuet-Higgins 1992) that the majority of bubbles have radii smaller than 2.5 mm. This is consistent with the subsurface video recordings in which individual bubbles of radius larger than 5 mm could only occasionally be detected in a cloud of smaller bubbles. We therefore conclude that only in rare cases when the sensor passes through larger air cavities of several centimeters diameter in plunging breakers, will the air temperature dominate the observed signal. These cases were recognized by the particular shape of the temperature signal as well as the video recording and were eliminated from the subsequent data analysis.

REFERENCES

Bortkovskii, R. S., 1987: *Air–Sea Exchange of Heat and Moisture during Storms.* D. Reidel, 194 pp.

Carslaw, H. S., and J. C. Jaeger, 1959: *Conduction of Heat in Solids.* 2d ed. Oxford Press, 510 pp.

Clauss, E., H. Hinzpeter, and J. Müller-Glewe, 1970: Messungen zur Temperaturstruktur im Wasser an der Grenzfläche Ozean–Atmosphäre. *Meteor. Forsch. Ergeb.,* **B5,** 90–94.

Cliff, R., J. R. Grace, and M. E. Weber, 1978: *Bubbles, Drops and Particles.* Academic Press, 380 pp.

Dobson, F. W., and S. D. Smith, 1988: Bulk models of solar radiation at sea. *Quart. J. Roy. Meteor. Soc.,* **114,** 166–182.

Efimova, N. A., 1961: On methods of calculating monthly values of net longwave radiation. *Meteor. Hydrol.,* **10,** 28–33.

Farmer, D. M., and M. Li, 1995: Patterns of bubble clouds organized by Langmuir circulation. *J. Phys. Oceanogr.,* **25,** 1426–1440.

——, C. L. McNeil, and B. D. Johnson, 1993: Evidence for the importance of bubbles in increasing air–sea gas flux. *Nature,* **361,** 620–623.

Hasse, L., 1971: The sea surface temperature deviation and the heat flow at the sea–air interface. *Bound.-Layer Meteor.,* **1,** 368–379.

Jessup, A. T., 1996: The infrared signature of breaking waves. *The Air–Sea Interface,* M. A. Donelan, W. H. Hui, and W. J. Plant, Eds., University of Toronto Press, in press.

Katsaros, K. B., 1976: Effects on precipitation on the eddy exchange in a wind driven sea. *Dyn. Atmos. Oceans,* **1,** 99–126.

——, 1980: The aqueous thermal boundary layer. *Bound.-Layer. Meteor.,* **18,** 107–127.

Keeling, R. F., 1993: On the role of large bubbles in air–sea gas exchange and supersaturation in the ocean. *J. Mar. Res.,* **51,** 237–271.

Kitaigorodskii, S. A., 1984: On the fluid dynamical theory of turbulent gas transfer across an air–sea interface in the presence of breaking waves. *J. Phys. Oceanogr.,* **14,** 960–972.

Koga, M., 1982: Bubble entrainment in breaking wind waves. *Tellus,* **34,** 481–489.

Lamarre, E., and W. K. Melville, 1991: Air entrainment and dissipation in breaking waves. *Nature,* **351,** 469–472.

——, and ——, 1992: Instrumentation for the measurement of void-fraction in breaking waves: Laboratory and field results. *IEEE J. Ocean Eng.,* **17,** 204–215.

Ling, C. S., 1993: Effect of breaking waves on the transport of heat and vapor fluxes from the ocean. *J. Phys. Oceanogr.,* **23,** 2360–2372.

Longuet-Higgins, M. S., 1992: The crushing of air cavities in a liquid. *Proc. R. Soc. London, Ser. A,* **439,** 611–626.

——, and J. S. Turner, 1974: An 'entraining plume' model of a spilling breaker. *J. Fluid Mech.,* **63,** 1–20.

McAlister, E. D., and W. L. McLeish, 1965: Oceanographic measurements with airborne infrared equipment and their limitations. *Oceanography from Space,* G. C. Ewing, Ed., Woods Hole Oceanogr. Inst. Ref. No. 65-10, 189–214.

Melville, W. K., and R. J. Rapp, 1985: Momentum flux in breaking waves. *Nature,* **336,** 54–59.

Olsen, H. O., 1967: Theoretical and experimental investigation of impedance void meters. Ph.D. thesis, University of Oslo, 141 pp.

Schluessel, P., W. J. Emery, H. Graβl, and T. Mammen, 1990: On the bulk skin temperature difference and its impact on satellite remote sensing of sea surface temperature. *J. Geophys. Res.,* **95,** 13 341–13 356.

Smith, S. D., 1981: Coefficients for sea surface wind stress and heat exchange. Bedford Institute of Oceanography Rep. Series/BI-R-81-19/Dec 1981, 31 pp.

Thorpe, S. A., 1982: On the clouds of bubbles formed by breaking wind-waves in deep water, and their role in air–sea gas transfer. *Philos. Trans. Roy. Soc. London, Ser. A,* **304,** 155–210.

——, 1993: Energy loss by breaking waves. *J. Phys. Oceanogr.,* **23,** 2498–2502.

——, and A. J. Hall, 1987: Bubble clouds and temperature anomalies in the upper ocean. *Nature,* **328,** 48–51.

Woolf, D. K., and S. A. Thorpe, 1991: Bubbles and air–sea gas exchange of gases in near saturation conditions. *J. Mar. Res.,* **49,** 435–466.